# Photoneutron cross-section measurements in the $^{209}$Bi($\gamma$,$xn$) reaction with a new method of direct neutron-multiplicity sorting

I. Gheorghe,[1,2] H. Utsunomiya,[3,*] S. Katayama,[3] D. Filipescu,[1,4] S. Belyshev,[5] K. Stopani,[6] V. Orlin,[6] V. Varlamov,[6] T. Shima,[7] S. Amano,[8] S. Miyamoto,[8] Y.-W. Lui,[9] T. Kawano,[10] and S. Goriely[11]

[1]*Extreme Light Infrastructure Nuclear Physics, "Horia Hulubei" National Institute for Physics and Nuclear Engineering (IFIN-HH), 30 Reactorului, Bucharest-Magurele 077125, Romania*

[2]*Department of Physics, University of Bucharest, Bucharest-Magurele 077125, Romania*

[3]*Department of Physics, Konan University, Okamoto 8-9-1, Higashinada, Kobe 658-8501, Japan*

[4]*"Horia Hulubei" National Institute for Physics and Nuclear Engineering (IFIN-HH), 30 Reactorului, Bucharest-Magurele 077125, Romania*

[5]*Department of Physics, Lomonosov Moscow State University, Moscow 119991, Russia*

[6]*Lomonosov Moscow State University, Skobeltsyn Institute of Nuclear Physics, Moscow 119991, Russia*

[7]*Research Center for Nuclear Physics, Osaka University, Suita, Osaka 567-0047, Japan*

[8]*Laboratory of Advanced Science and Technology for Industry, University of Hyogo, 3-1-2 Kouto, Kamigori, Ako-gun, Hyogo 678-1205, Japan*

[9]*Cyclotron Institute, Texas A&M University, College Station, Texas 77843, USA*

[10]*Los Alamos National Laboratory, Los Alamos, New Mexico 87545, USA*

[11]*Institut d'Astronomie et d'Astrophysique, Université Libre de Bruxelles, Campus de la Plaine, CP-226, 1050 Brussels, Belgium*

(Received 28 June 2017; published 6 October 2017)

Photoneutron cross sections were measured in the $^{209}$Bi($\gamma$, $xn$) reaction with $x = 1$–4 at energies from the neutron threshold to 40 MeV using quasimonochromatic laser Compton-scattering $\gamma$-ray beams. A novel technique of direct neutron-multiplicity sorting with a flat-efficiency detector was used. Results are compared with the positron in-flight annihilation data of Livermore and Saclay as well as with bremsstrahlung data. The present neutron yields are consistent with the latest photoactivation measurement with bremsstrahlung. The giant dipole resonance component of the total photoneutron cross section is reasonably reproduced by model calculations of the Hartree-Fock Bogoliubov plus quasiparticle random phase approximation based on the Gogny D1M interaction for both E1 and M1 components. In contrast, the quasideuteron component of the total photoneutron cross section requires a factor of ∼3 enhancement of the Levinger parameter. Furthermore, a survival of large ($\gamma$,$n$) cross sections above 20 MeV may indicate the surface effect on the two-component particle-hole state density. The threshold behavior of photoneutron emission is discussed in terms of the average neutron kinetic energy.

DOI: 10.1103/PhysRevC.96.044604

## I. INTRODUCTION

Photonuclear data, describing the interaction of photons with atomic nuclei, are used both in fundamental nuclear studies and in a wide variety of applications. A large fraction of the data was measured using positron annihilation in-flight $\gamma$-ray beams during the 1960s and 1970s at the Lawrence Livermore National Laboratory (USA) and the Centre d'Etudes Nucleaires de Saclay (France) facilities and compiled in the atlas [1]. These pioneering works have formed a foundation of our understanding of the strongest collective motion in the nuclear system, isovector giant dipole resonance (GDR). The user community currently relies on the Photonuclear Data Library generated in 2000 by the International Atomic Energy Agency (IAEA) [2], containing the compilation and evaluation of the then-existing photonuclear data. It is widely recognized that there are large discrepancies between the Livermore and Saclay data of total and partial photoneutron cross sections. Generally, the photoneutron yield cross sections measured at the two laboratories disagree by 10%–15%, while greater differences up to 30%–40% have been observed for the partial ($\gamma$,$n$) and ($\gamma$,$2n$) cross sections [3].

A new coordinated research project has been launched by the IAEA to update the current photonuclear data library [4]. One of its main objectives is to provide new total and partial photoneutron cross sections for selected nuclei to resolve the longstanding discrepancies between the Livermore and Saclay data. Although many new photoneutron studies have been performed using the intense, monochromatic laser Compton scattering (LCS) $\gamma$-ray beams recently available at the TERAS [5–19], NewSUBARU [20–24], and HI$\gamma S$ [25] facilities, the measurements were limited in energy below the double-neutron emission threshold.

Recently, a new method of direct neutron multiplicity (DNM) sorting has been developed [26], which, in combination with several to tens of MeV LCS $\gamma$-ray beams, allows complete mapping of the photoneutron reaction cross sections within the GDR energy range. The authors have committed to a series of ($\gamma$,$xn$) cross-section measurements with the DNM sorting method for $^{9}$Be, $^{59}$Co, $^{89}$Y, $^{103}$Rh, $^{139}$La, $^{159}$Tb, $^{165}$Ho, $^{169}$Tm, $^{181}$Ta, $^{197}$Au, and $^{209}$Bi in the IAEA-CRP on updating the photonuclear data library.

We applied the technique for the first time on $^{209}$Bi, a natural mono-isotopic element with possible applications in

*Corresponding author: hiro@konan-u.ac.jp

 

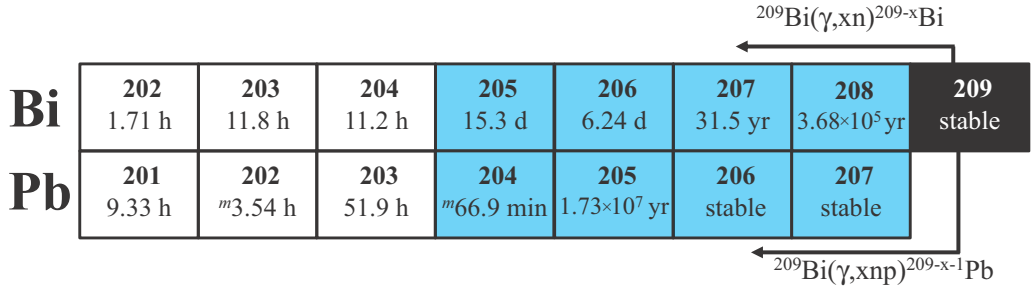


FIG. 1. An excerpt of the chart of nuclei depicting our $^{209}$Bi$(\gamma,xn)$ measurements with $x = 1$–4. The residual nuclei of the induced reactions are marked by blue background. Both the $(\gamma,xn)$ and $(\gamma,xnp)$ reactions were induced, populating the $^{205-208}$Bi and the $^{204-207}$Pb isotopes.

accelerator-driven systems (ADS). As a lead-bismuth eutectic alloy is proposed and investigated as spallation target and coolant material [27], nuclear reactions, which lead to neutron multiplication in Pb and Bi are directly influencing the neutron economy in the reactor. Such is the case of photoneutron reactions, which are triggered by high-energy photons emitted both in spallation and fission reactions.

Also, the need for reliable information on photoneutron reactions on $^{209}$Bi has been identified in relation with ADS in-core neutron dosimetry measurements. The $^{209}$Bi$(n,3n)^{207}$Bi reaction has been recently included in the IAEA International Reactor Dosimetry and Fusion File [28] and the $^{209}$Bi$(n,4-8n)$ reactions are being investigated for neutron fluence monitoring and spectrum unfolding at the high-energy accelerator-driven neutron sources. Bismuth is suitable for neutron dosimetry because it has high neutron nonelastic and neutron emission cross sections and, as can be observed in Fig. 1, the $^{201-207}$Bi isotopes obtained as residual nuclei in the dosimetric reactions have half-lives suitable to activation measurements. For neutron and gamma fields, the competition between the photoneutron $^{209}$Bi$(\gamma,2-7n)$ reactions and the neutron induced $^{209}$Bi$(n,3-8n)$ reactions which produce the same residual isotope must be taken into consideration using proper and reliable nuclear data.

The photoneutron yield reaction cross section on $^{209}$Bi has been measured using quasimonochromatic $\gamma$-ray beams produced in positron in flight annihilation both at the Saclay [29] and Livermore [30] facilities. The discrepancy between the two measurements is about 10–20% and is most significant for the cross section around the GDR peak energy. Also, existing bremsstrahlung measurements [31] provide a GDR centroid energy shifted towards lower energies. Our earlier work [32] provided yields of multiparticle photonuclear reactions on $^{209}$Bi using bremsstrahlung beams with end-point energy 55.6 MeV and the photoactivation technique. In the present work, we have determined the cross sections of the $^{209}$Bi$(\gamma,xn)$ reactions with $x = 1$–4 using LCS $\gamma$-ray beams with energies between 7.6 and 40 MeV and compared them with these previous measurements.

## II. EXPERIMENTAL PROCEDURE

Photoneutron cross-section measurements were performed in $^{209}$Bi$(\gamma,xn)$ reactions with $x = 1$–4 using LCS $\gamma$-ray beams at the NewSUBARU synchrotron radiation facility [20]. A schematic diagram of the experimental setup is shown in Fig. 2. The beam irradiated a $^{209}$Bi target placed at the center of a $^{3}$He neutron detection system. The $\gamma$-ray beam energy spread and flux were monitored using large volume lanthanum bromide ($LaBr_3$:Ce) and NaI detectors, respectively.

The data were written in a triggerless list mode, using an eight-parameter 25 MHz digital data acquisition (DAQ) system. The system collected the energy signals from the $LaBr_3$:Ce and NaI detectors, along with the time of neutrons being recorded in the $^{3}$He counters. The time of laser photon bunch release, provided by an external clock signal applied to the laser, was also collected by the DAQ system and used as a time reference for constructing event mode structured data files.

As the experimental method employed here is based on the direct detection of outgoing neutrons, we measured the sum cross section of all reactions, which contribute to the production of $x$ reaction neutrons, where $x = 1$–4. Thus, for simplicity of notation, we refer throughout the paper to the $[(\gamma,xn)+(\gamma,xnp)+(\gamma,xn2p)+\cdots]$ combined reactions simply as $(\gamma, xn)$, with $x = 1$–4. We present here details about the $\gamma$-ray beam production and monitorization, neutron detection system, and target preparation.

### A. $\gamma$-ray beam production and measurement

The high-power Nd:$YVO_4$ laser INAZUMA (Spectra-Physics) was used to produce LCS $\gamma$-ray beams with maximum energies between 7.7 and 42.2 MeV. The laser was operated in Q-switch mode at 16.66 kHz frequency, corresponding to a 60 $\mu$s time interval between consecutive laser bunches. Electron beams at 982 MeV were injected into the ring up to the maximum current of 300 mA. A top-up operation, in which the current was kept constant, was applied for the injection energy.

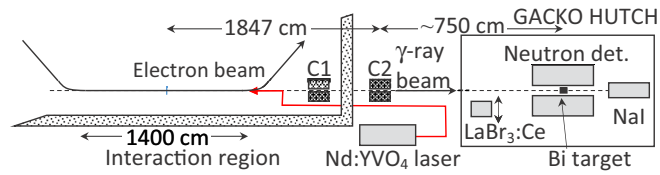


FIG. 2. The $\gamma$-ray beam line at the NewSUBARU synchrotron radiation facility.

For the high-energy region, between 14.3 and 42.2 MeV in the maximum energy of the $\gamma$-ray beam, the laser was operated in the second harmonic ($\lambda = 532$ nm; power = 14 W) and the electron beam energy was varied in deceleration mode from 982–640 MeV and in acceleration mode from 982–1108 MeV. For the low-energy region, below the double-neutron emission threshold ($S_{2n} = 14.35$ MeV), the laser was operated in the fundamental mode ($\lambda = 1064$ nm; power = 35 W) and had a pulsed, 10 Hz macroscopic time structure, of 80 ms beam-on and 20 ms beam-off. The electron beam energy was varied in deceleration mode between 902 and 660 MeV.

The $\gamma$-ray beam line is, as shown in Fig. 2, a 14 m long straight section of the storage ring inside which the laser beam was directed head-on against the electron beam. The photon scattering angle was limited to ~0.05 mrad using two 10 cm thick lead collimators with six (C1) and two (C2) mm openings in diameter in order to produce quasimonochromatic $\gamma$-ray beams.

The energy of the $\gamma$-ray beams was beyond the range of standard calibration sources. Therefore, the absolute value for the maximum energy of the LCS beams was obtained by relying on the precise knowledge of the laser photon and electron beam energies. The energy of the NewSUBARU electron beam is characterized by 0.4% resolution and has been calibrated between 0.5 and 1.5 GeV with an accuracy of the order of $10^{-5}$ [33,34].

Measurements of the $\gamma$-ray beam energy profile were performed with a 3.5 in × 4 in $LaBr_3$:Ce detector for each $\gamma$-ray beam energy before and after each target irradiation with the laser operated in the continuous-wave mode at a reduced power in order to avoid pileup effects. The Compton backscattering of laser photons on relativistic electrons and the electromagnetic interactions of the $\gamma$-ray beams inside the collimators and the $LaBr_3$:Ce detector were simulated using the GEANT4 Monte Carlo code [35]. The laser beam was implemented as a continuous Gaussian beam using the spatial distribution parameters published in Ref. [36]. A continuous electron beam was described using realistic Twiss parameters and emittance, where a Gaussian emittance profile was considered. For each irradiation point, the values for the electron beam emittance and spot size at the focal point were iteratively adjusted starting from the values published in Refs. [36,37], until the experimental $LaBr_3$:Ce detector response was reproduced by the GEANT4 simulation.

Typical spectra of the LCS $\gamma$-ray beams recorded with the $LaBr_3$:Ce detector along with the GEANT4 simulations of the detector response function and incident $\gamma$-ray beam are displayed in Fig. 3. The experimental response functions are well reproduced by the GEANT4 simulations. Energy spreads of 2.4%, 1.6%, and 2% in the full width at half maximum (FWHM) were obtained for the three incident $\gamma$-ray beams at 15.4, 29.9, and 37.4 MeV in the maximum energy, respectively. Reliable simulations of incident LCS $\gamma$-ray beam spectra are needed for obtaining the average photon energy and the fraction of incident photons above given reaction thresholds and for the unfolding of the raw cross sections (see details in Sec. III B). For example, for the 15.4 MeV maximum energy photon beam displayed in Fig. 3(b), 99.7% of the photons have energies higher than the single-neutron emission threshold

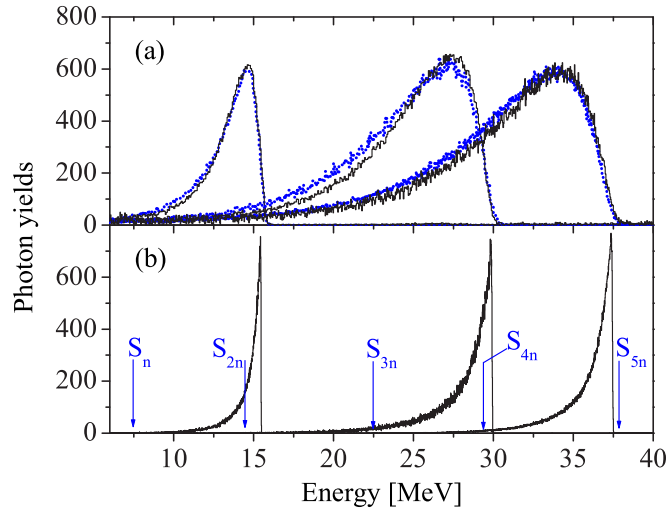


FIG. 3. (a) shows typical spectra of the $\gamma$-ray beams recorded with the $LaBr_3$:Ce detector (solid black lines) and the simulations of the response function (dotted blue lines), while the corresponding incident $\gamma$-ray beam spectra are displayed in (b). The threshold values for the emission of one ($S_n = 7.46$ MeV), two ($S_{2n} = 14.3$ MeV), three ($S_{3n} = 22.4$ MeV), four ($S_{4n} = 29.5$ MeV), and five ($S_{5n} = 37.8$ MeV) neutrons are displayed by blue arrows in (b).

($S_n$) at 7.46 MeV and their average energy is 14.51 MeV, while only 71% of them have energies higher than the double-neutron emission threshold ($S_{2n}$) and their average energy is of 15.07 MeV. Energy resolution between 1.6% and 3.2% in FWHM was obtained for the high energy $\gamma$-ray beams, above the $S_{2n}$. The low energy $\gamma$-ray beams below the $S_{2n}$ showed a broader energy spread of 4%–7%.

The $\gamma$-ray beam flux was monitored during each irradiation with a large volume (8 in × 12 in) NaI(Tl) detector placed inside the $\gamma$-ray beam dump. An example of a stable 23.9 MeV $\gamma$-ray beam current obtained at the 831 MeV electron beam energy is shown in Fig. 4(a). While the electron beam was stable in the deceleration mode, sudden drops of the beam current, which generate $\gamma$ and neutron flashes, took place several times during the LCS $\gamma$-ray irradiation in the acceleration mode. The events corresponding to the sudden drops were identified event-by-event by monitoring the time profile of the $\gamma$-ray flux and removed in the offline analysis.

The neutron coincidence measurements above the $S_{2n}$ required a time interval between consecutive $\gamma$-ray bunches comparable to the moderation time of neutrons inside the polyethylene block. Therefore, the 60 $\mu$s interval provided by the INAZUMA laser was extended to 480 $\mu$s by modulating the laser beam intensity. For this, an additional optical system comprised of a Pockels cell and a polarizer was used to block seven out of eight consecutive laser pulses. The working parameters of the optical system were tuned to maximize both the transmission for allowed laser components and the stopping power for the blocked laser components. Figure 4(b) shows a time spectrum of a 23.9 MeV incident LCS $\gamma$-ray beam, where the time is relative to the preceding clock signal. The high-amplitude peak in the vicinity of 0 $\mu$s represents the main LCS $\gamma$-ray bunches, corresponding to the allowed laser pulses. The low-amplitude peaks with the 60 $\mu$s time intervals

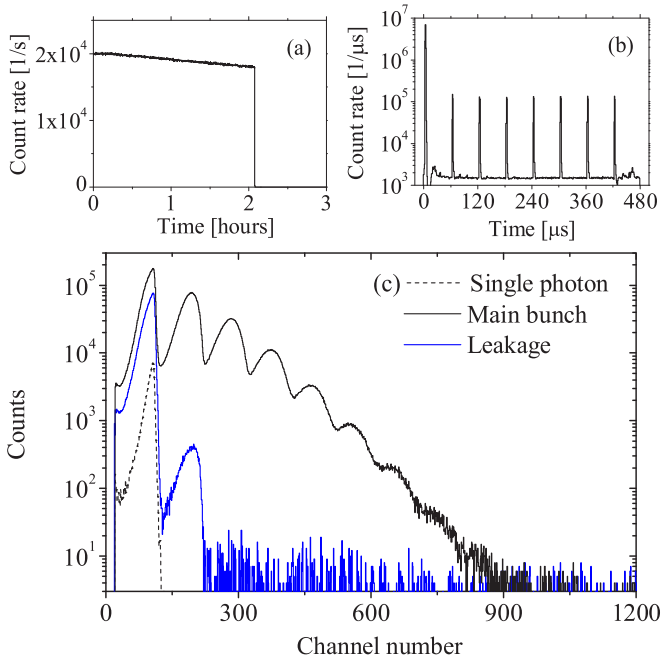


FIG. 4. Time and energy spectra of incident 23.9 MeV LCS $\gamma$-ray beam recorded with the NaI(Tl) detector. (a) Time variation of the $\gamma$-ray count rate. (b) Time structure of the $\gamma$-ray beam relative to the preceding main $\gamma$-ray bunch. (c) Multiphoton energy spectra generated by main-bunch (solid black) and leakage (solid blue) contributions and single photon spectrum (dashed).

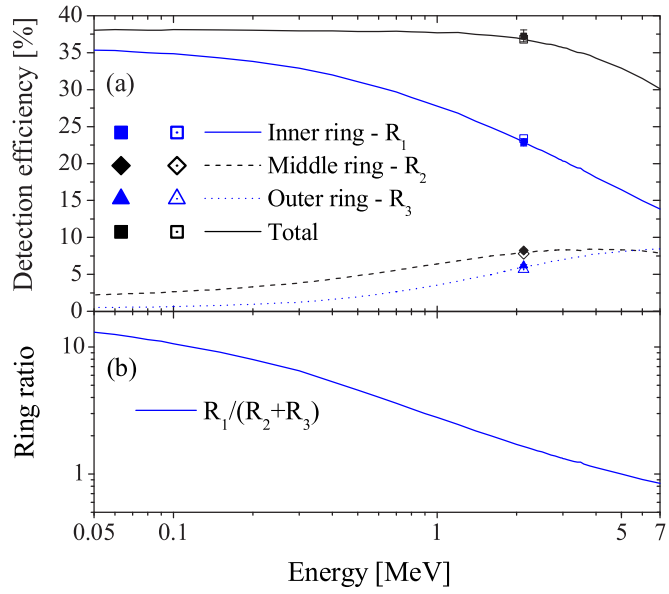


FIG. 5. (a) The detection efficiencies of the inner (R1), middle (R2), and outer (R3) counter rings and the total efficiency, as follows: MCNP simulations for neutron evaporation spectra (lines), experimental values obtained using a calibrated $^{252}$Cf source (full symbols), MCNP simulations for $^{252}$Cf neutron spectrum (empty symbols). (b) The ring ratio for the neutron detection system. See text for details.

represent the leakage LCS $\gamma$-ray bunches, corresponding to the partially blocked laser pulses.

As described in Ref. [21], LCS $\gamma$ rays are generated in bunches corresponding to each laser light pulse following a Poisson probability distribution. During the irradiation, the NaI(Tl) detector recorded multiphotons from the same $\gamma$-ray bunch and so-called multiphoton (pileup) spectra were generated. Before the irradiation, single-photon spectra were measured by operating the laser at reduced power. The number of recorded $\gamma$ photons was obtained by unfolding the multiphoton spectrum with the single-photon spectrum, as described in Refs. [21,38]. The attenuation in the targets and NaI detector were taken into account. The NaI(Tl) detector registered 98.2%–99.7% of the total incident photon flux, depending on the $\gamma$-ray beam energy. The photon attenuation in the targets is discussed in Sec. II C.

In the data analysis, we compute the number of reactions induced by the main bunch photons and treat the leakage photons as background. Thus, the procedure described above is applied on the multiphoton spectra generated by the main-bunch contribution, which was isolated by gating on the main-bunch peak in the NaI(Tl) time spectrum [Fig. 4(b)].

A typical example of the experimental multiphoton and single-photon spectra is shown in Fig. 4(c), where the main-bunch and leakage components are displayed separately. The main LCS $\gamma$-ray spectrum displays a Poisson distribution with the average photon-multiplicity of 1.9 photons per bunch, while the partially blocked leakage component is characterized by 1.01 photons per bunch. The number of leakage $\gamma$ rays account for 9% of the total number of LCS photons. Throughout the measurements, this ratio was kept below 10%.

### B. Neutron detection

The neutrons emitted from the $^{209}$Bi target were recorded using a detection array comprised of three concentric rings of 4, 9, and 18 $^{3}$He counters (10 atm) located at 5.5, 13.0, and 16.0 cm from the $\gamma$-ray beam axis, respectively. The counters were embedded in a polyethylene moderator block shielded by additional borated polyethylene plates for background neutron suppression. Simulations of neutron detection efficiencies were performed using the MCNP [39] simulation package considering $s$-wave evaporation neutron sources placed at the center of the moderator. The evaporation spectra were calculated based on the Weisskopf-Ewing model [40].

The detection efficiency was measured to be $37.27 \pm 0.82\%$ at 2.13 MeV, the average energy of the $^{252}$Cf neutron spectrum corresponding to a Maxwellian temperature of 1.42 MeV. The measurement was performed with a $^{252}$Cf source whose absolute emission rate of $(1.62 \pm 0.04) \times 10^4$ neutrons per second was calibrated at the National Metrology Institute of Japan. As shown in Fig. 5(a), the experimental calibration is well reproduced by the MCNP simulations with the Weisskopf-Ewing evaporation spectra and the $^{252}$Cf neutron spectrum. All simulation results are displayed at the average neutron energies. The neutron detection efficiency of the flat-response detector averaged over 10 keV–5 MeV is $36.5 \pm 1.6\%$, where the uncertainty represents one standard deviation.

Below the double-neutron emission threshold, each ring of $^{3}$He counters was connected to a logical electronic

system that generated signals on the OR condition, after applying an amplitude threshold for neutron-$\gamma$ discrimination. For each irradiation point, the neutron detection efficiency was determined using the ring-ratio technique described in Refs. [16,41]. The ring ratio simulated for the flat-efficiency neutron detector is displayed as a function of neutron energy in Fig. 5(b). The experimental ring ratios were obtained as the ratio between the number of reaction neutrons recorded by the inner ring (R1) and the sum of reaction neutrons recorded by the middle (R2) and outer (R3) rings. The detection efficiency varied by 1.4% between 36.5% and 37.9% over the relevant neutron energy range. The deduced average neutron energies are discussed in Sec. V.

Above the double-neutron emission threshold, the ring-ratio technique cannot directly determine the average neutron energies for individual $(\gamma,xn)$ reactions [26]. The relevant neutron energy range was investigated [26] using a Monte Carlo (MC) statistical model code [42]. The MC calculation provided energy distributions of neutrons successively emitted in each $^{209}$Bi$(\gamma, xn)$ reaction channel for incident photon energies up to 40 MeV, resulting in average neutron energies below 5 MeV. Therefore, the efficiency of the flat-response neutron detector averaging over 10 keV to 5 MeV ($36.5 \pm 1.6\%$) was used. We remark that the neutron spectra summed over all the $^{209}$Bi$(\gamma, xn)$ reaction channels provided by the MC code are in good agreement with those provided by the standard statistical model codes such as TALYS [43] and EMPIRE [44].

### C. Target preparation

Cylindrical metallic samples of $^{209}$Bi in aluminum target holders placed at the center of the flat-response neutron detector were irradiated with the LCS $\gamma$-ray beam. A 20 mm (diameter) $\times$ 4 mm (thickness) sample with 3.947 g/cm$^2$ areal density was used for the measurements below the $S_{2n}$. The photon attenuation in the target varied from 16.9%–20.1% and was calculated using the mass attenuation coefficients tabulated in Ref. [45]. For the higher-energy measurements up to 37.4 MeV $\gamma$-ray energy, a thicker 12 mm $\times$ 7 mm sample of 6.969 g/cm$^2$ areal density was used. The photon attenuation in the target varied between 33.5% and 41.2%. A 12 mm $\times$ 10 mm sample of 9.796 g/cm$^2$ areal density was used for the 42.2 MeV $\gamma$-ray beam energy measurement, corresponding to 54.1% photon attenuation in the target. The areal density of each target was computed as the product of the measured target thickness and the 9.747 g/cm$^3$ material density tabulated in Ref. [46]. The sample thickness was chosen in appropriate combination with the incident $\gamma$-ray flux and reaction cross sections to minimize multiple firings of photoneutron reactions by a single pulse of $\gamma$ rays in the target.

## III. DATA ANALYSIS

### A. Number of induced reactions

Below the double-neutron emission threshold, the number of induced reactions is equal to the number of emitted neutrons. The 10 Hz time structure of 80 ms beam-on and 20 ms beam-off allowed a simple subtraction of background neutrons for each irradiation point.

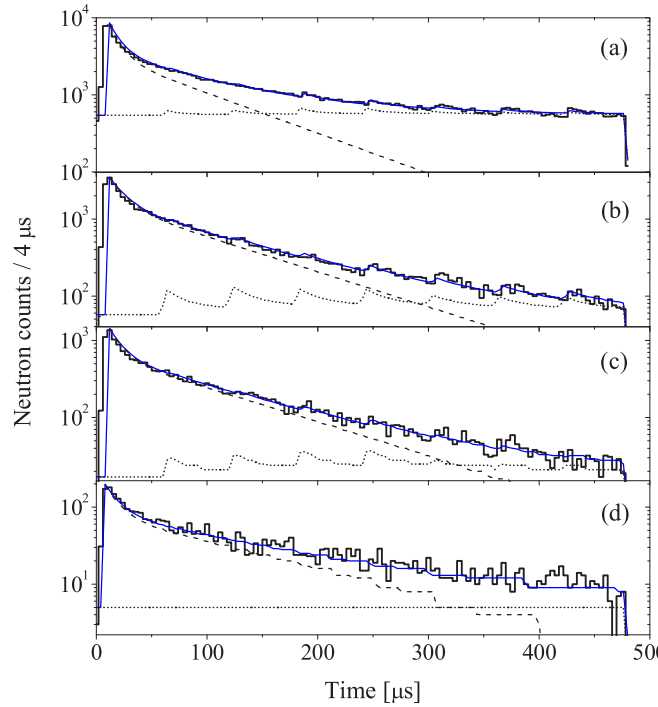


FIG. 6. Neutron moderation time spectra of (a) single, (b) double, (c) triple, and (d) quadruple neutron events generated in $^{209}$Bi$(\gamma,xn)$ reactions induced by 42.2 MeV maximum energy LCS $\gamma$-rays. The experimental time spectra (solid black) are displayed along with the corresponding best fit (solid blue). The fit functions for reaction neutrons (dashed) produced by the main $\gamma$-ray bunches and the background (dotted) contributions are displayed separately.

Above the double-neutron emission threshold, the number of events in which only one (single $N_1$), only two (double $N_2$), only three (triple $N_3$), and only four (quadruple $N_4$) neutron events were recorded, were determined from the neutron moderation time spectra.

Figure 6 shows examples of neutron time moderation spectra for single ($N_1$), double ($N_2$), triple ($N_3$), and quadruple ($N_4$) events, respectively. The spectra are comprised of eight neutron moderation components 60 $\mu$s apart from each other. The first one with the highest amplitude corresponds to the reactions induced by the main $\gamma$-ray bunch. The following seven components with low amplitudes correspond to reactions induced by the leakage $\gamma$-ray bunches.

Each component was fitted using a sum of two exponential functions:

$$h_x(t) = A_{1x} \cdot \exp\left(\frac{xT - t}{\tau_{1x}}\right) + A_{2x} \cdot \exp\left(\frac{xT - t}{\tau_{2x}}\right), \quad (1)$$

where $x$ is the index of the component (0 for the main $\gamma$-ray bunch and 1–7 for the leakage components), and $T$ is the 60 $\mu$s interval between two successive bunches. The total experimental spectrum is therefore fitted using:

$$h(t) = B + \sum_{x=0}^{x=7} h_x(t), \quad (2)$$

where $B$ is a constant background component.

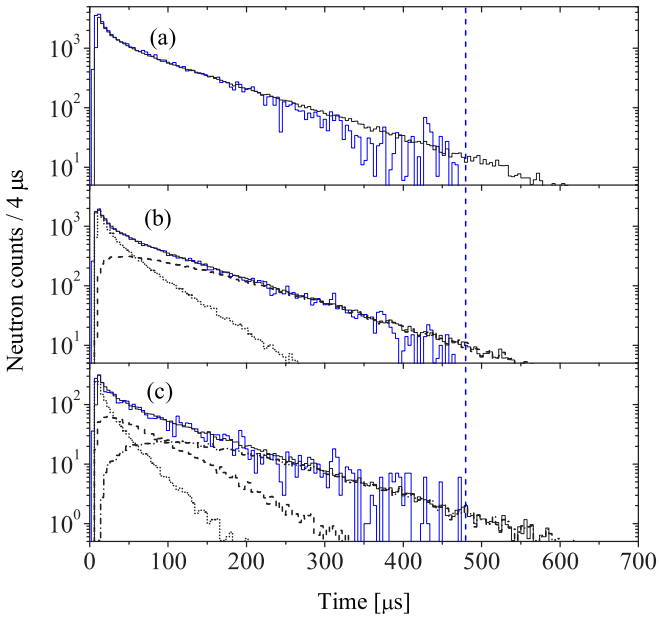


FIG. 7. Comparison between experimental (solid blue) and simulated (solid black) time spectra of neutrons emitted in $^{209}$Bi($\gamma$,$xn$) reactions for incident photon energy of 29 MeV and recorded by the neutron detection system. The spectra are obtained by applying coincidence conditions of (a) one, (b) two, and (c) three recorded neutrons during the same event.

The number of neutron $j$-fold coincidence events, $N_j$ with $j = 1$–4, for reactions induced by the main $\gamma$-ray bunches, was computed by subtracting the background and leakage components from the total number of neutrons recorded in $j$-fold coincidence events, $N_j^{\mathrm{tot}}$:

$$N_j = \frac{1}{j} \cdot \left[ N_j^{\mathrm{tot}} - \int Bdt - \sum_{x=1}^{x=7} \int h_x(t)dt \right]. \quad (3)$$

The effect of using the finite time range of 480 $\mu$s was investigated using GEANT4 simulations of neutron transportation through the detection system. The simulation includes neutron elastic and inelastic scattering, neutron capture, and additional thermal neutron scattering on polyethylene molecules with possible excitation of vibrational modes. The simulation is tuned so as to reproduce results of a measurement carried out with the $^{252}$Cf calibrated source. Realistic $^{209}$Bi($\gamma$, $xn$) neutron sources have been implemented in the GEANT4 simulation based on the results of the MC code described in Sec. II B.

Figure 7 shows simulated and background subtracted experimental time spectra of neutrons emitted in $^{209}$Bi($\gamma$,$xn$) reactions at 29 MeV. Time spectra simulated for the first (dotted), second (dashed), and third (dashed dotted) arriving neutrons are also shown in the figure. Small fractions of the second-arriving neutrons in the double-neutron events and the third-arriving neutrons in the triple-neutron events are missed by applying the 480 $\mu$s time gate as well as those in the single-neutron events. It was found that a misassignment of the $j$-fold events ($j = 1$–4) caused by the small fractions beyond 480 $\mu$s is no more than a few percent. This percentage does not change as a function of the photon energy between the two- and five-neutron emission thresholds.

The direct neutron multiplicity sorting technique (DNM) described in Ref. [26] was applied to obtain the number of $^{209}$Bi($\gamma$, $xn$) reactions with $x = 1$–4. For each irradiation point, the numbers of ($\gamma$, $xn$) reactions, $R_x$, were obtained by solving the following set of equations:

$$N_j = \sum_{i=j}^{m} {}_iC_j \cdot R_i \cdot \varepsilon^j (1-\varepsilon)^{i-j}. \quad (4)$$

Here, $N_j$ is the number of $j$-fold neutron events computed using Eq. (3), $m$ is the maximum neutron multiplicity, ${}_iC_j$ is the combinatorial factor, $\varepsilon$ is the neutron detection efficiency, $j$ is the number of neutrons detected, and $i - j$ is the number of neutrons undetected.

The uncertainty of the number of ($\gamma$, $xn$) reactions $R_x$ ($x = 1$–4) was estimated in the error analysis in solving Eq. (4), where not only the statistical uncertainties of the numbers of $j$-fold events $N_j$ but also the systematic uncertainty of the neutron detection efficiency $\varepsilon$ (5.1%), which is a quadratic sum of 4.4% for the energy dependence of the efficiency and 2.5% for the absolute emission rate of the calibrated $^{252}$Cf source, were propagated.

### B. Reaction cross-section data

The photoneutron cross section measured experimentally is expressed as

$$\sigma_{\gamma xn}^{\mathrm{mono}} = \frac{R_x}{N_t N_\gamma \xi f_x}, \quad (5)$$

where $R_x$ represents the number of ($\gamma$,$xn$) reactions, $N_t$ gives the number of target nuclei per unit area, $N_\gamma$ is the number of incident $\gamma$ rays on the target and $\xi = [1 - \exp(\mu t_t)]/(\mu t_t)$ is a correction factor for a thick target measurement. The $f_x$ factor is the fraction of $\gamma$ flux above the $x$-neutron emission threshold, $S_{xn}$. We consider this to be the monochromatic approximation of the reaction cross section, hence the $\sigma_{\gamma xn}^{\mathrm{mono}}$ notation.

Low reaction rates are required for DNM sorting experiments to avoid double firings of two separate reactions on two nuclei induced by a given photon pulse. Using the experimental values for the monochromatic reaction cross sections, the average number of photons per $\gamma$-ray bunch in the Poisson distribution, target characteristics, and neutron detection efficiency, we computed for each irradiation point the number of induced reactions (true) and the number of coincidence events. We applied the set of Eq. (4) on the simulated number of events and obtained the calculated number of induced reactions. The correction factors were deduced as the ratios between the true and the calculated numbers of induced reactions and applied to the experimental cross sections.

The corrected (open circles) and uncorrected (open triangles) cross sections are compared in Fig. 8. The applied corrections are within the reactions cross section error bars for all measured points. The peak cross sections for all measured reactions channels are varied by 0–2%. The corrections are significant only for weak reaction channels measured along with stronger ones.

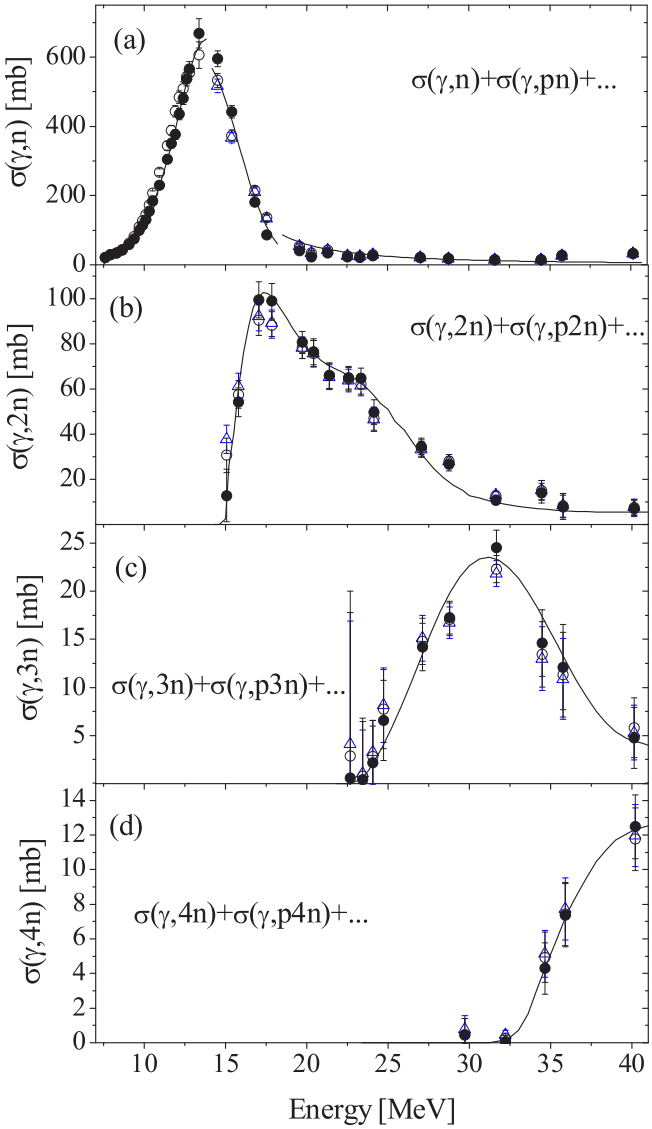


FIG. 8. The multiple-firing effect uncorrected (open triangles) and corrected (open circles) monochromatic and the nonmonochromatic $^{209}$Bi$(\gamma,xn)$ cross sections, where (a) $x = 1$, (b) $x = 2$, (c) $x = 3$, and (d) $x = 4$. The energy dependence functions used for applying the unfolding methods are also displayed (solid curves).

For example, after correction, the $(\gamma,2n)$ reaction cross sections decrease by 18%, 6%, and 2% for the first three energies above the $S_{2n}$, at 15.1, 15.8, and 17.0 MeV, respectively. For these three irradiation points, the fraction of double firings of two $(\gamma,n)$ reactions by the same bunch is 2% of the total number of $(\gamma,n)$ reactions, but the fraction accounts to 19%, 5%, and 1.5% of the total number of $(\gamma,2n)$ reactions. The effect is proportional to the difference between the $(\gamma,2n)$ and $(\gamma,n)$ reaction cross sections.

The next step was to take into account the measured energy distribution of the $\gamma$-ray beam. Such a treatment is especially important for the energy regions where the cross section varies significantly within the energy spread of the beam.

The monochromatic approximation of the reaction cross sections obtained as described above, represents the folding between the reaction cross section, $\sigma_{\gamma xn}(E)$, and the photon energy distribution of the $\gamma$-ray beam, $n(E)$:

$$\sigma_{\gamma xn}^{\text{mono}} = \int n(E)\sigma_{\gamma xn}(E)dE. \quad (6)$$

The incident photon energy distribution $n(E)$ for each irradiation point was obtained as described in Sec. II A. Starting from a trial function, iterative procedures have been applied to obtain the energy dependence of the reaction cross section, $\sigma_{\gamma xn}(E)$, needed for the unfolding of the measured reaction cross sections.

The $(\gamma,n)$ cross section was unfolded using the Taylor expansion method described in Ref. [21], where the trial cross section, $\sigma_{\gamma n}(E)$, was expanded in the Taylor series at the average energy $E_{\text{av}}$. The Taylor expansion method requires analytical functions for describing the trial cross section. A Lorentzian dependence with threshold behavior given in Ref. [21] was assumed below $S_{2n}$, the Gaussian formula was used for the energy interval between $S_{2n}$ and 18 MeV and a simple Lorentzian function was assumed above 18 MeV. The trial cross section was iteratively adjusted, starting with a best fit to the monochromatic cross section having the centroid energy, cross section, and width as free parameters and ending with a reasonable conversion. The overall correction varied between 0.1%–35%. The fit functions and the unfolded $(\gamma,n)$ reaction cross sections are displayed in Fig. 8(a).

The trial cross section required for unfolding the $(\gamma,xn)$ with $x = 2$–4 cross sections was obtained by reproducing the experimental cross sections in monochromatic approximation. The trial cross sections were iteratively adjusted until the global deviation between the calculated foldings $\int \sigma_t(E)n(E)dE$ and the monochromatic cross sections was minimized. The starting point for the trial $(\gamma,2n)$ cross sections was represented by a spline fit to the monochromatic cross section. The trial cross section was iteratively adjusted by multiplication with a third-order polynomial function. The trial $(\gamma,3n)$ and $(\gamma,4n)$ cross sections were assumed to be third-order polynomials, with a best fit to the monochromatic cross section as starting point. This process resulted in the unfolded cross sections shown in Figs. 8(b)–8(d), along with the monochromatic cross sections and the final trial function used for unfolding. The overall correction remained small, i.e., 0%–22% and within the error bars, except for the data points in the vicinity of the reaction thresholds. Because of the sharp rise above the $S_{2n}$, the first two $(\gamma,2n)$ data points are significantly affected.

As described in Sec. III A, the systematic uncertainty of the neutron detection efficiency was incorporated into the error propagation in estimating the uncertainty of the number of $(\gamma,xn)$ reactions, $R_x$. Thus, the remaining systematic uncertainty is 3.0% for the flux of the LCS $\gamma$-ray beam [38].

## IV. COMPARISON WITH PREVIOUS MEASUREMENTS

First, we compare the present data with positron in-flight annihilation ones measured at Saclay [29] and at Livermore [30] and with bremsstrahlung [31] data. The neutron

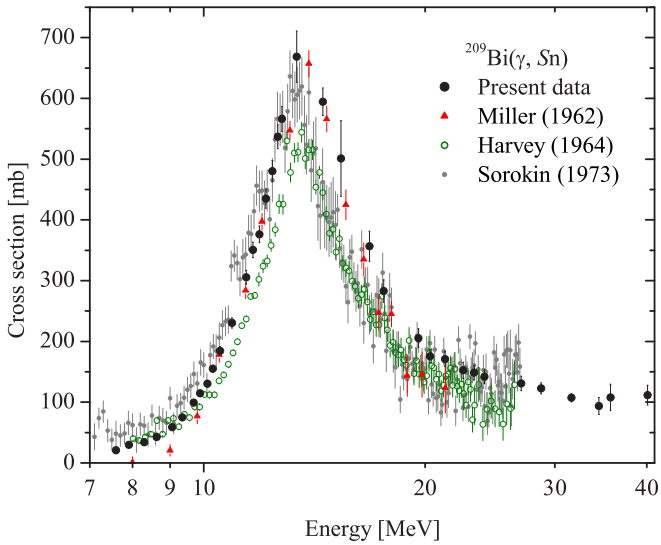


FIG. 9. Comparison between present data and existing positron in flight annihilation [29,30] and bremsstrahlung [31] data on the neutron yield cross section, $\sigma(\gamma,Sn)$.

yield cross section defined as $\sigma(\gamma,Sn) = \sum_{x=1}^{4} x\sigma(\gamma,xn)$ was measured below the $S_{3n}$ threshold by all three experiments, where only Refs. [30,31] provide separately the $(\gamma,n)$ and $(\gamma,2n)$ channels. Both the present LCS and the existing positron in-flight annihilation and bremsstrahlung data include the charged particle emission channels and can be directly compared, without any approximations or asumptions made on the charged particle emission contribution.

As can be seen in Fig. 9, the Livermore cross sections [30] are generally lower than the present ones, except for the 8–10 MeV energy region where we obtained similar results. The present measurements are in good agreement with the Saclay data [29] around the GDR peak energy, concerning both the height of the GDR Lorentzian and its width. Below 10 MeV and above 18 MeV, the Saclay cross sections have significantly lower values than the present ones. We note that, compared to the positron in-flight annihilation and the present data, the bremsstrahlung cross sections [31] are slightly shifted by ~0.5 MeV towards lower energies. Having in mind a possible energy shift generated by the bremsstrahlung data unfolding procedure, the present measurements are in relatively good agreement with the bremsstrahlung ones within the entire energy region of 7–26 MeV, with slightly higher cross sections around the GDR peak energy.

Second, we compare the present results with the activation yields measured using bremsstrahlung photon beams with 55.6 MeV end-point energy [32] at the Skobeltsyn Institute of Nuclear Physics (MSU) [47]. The $(\gamma, 2-6n)$, $(\gamma, 4np)$, and $(\gamma, 5np)$ reaction yields on $^{209}$Bi were obtained in the MSU experiment using the activation technique. For the comparison, we computed spline fits of the present $(\gamma, 2-4n)$ cross sections, extrapolated them up to 55.6 MeV, and folded them with the bremsstrahlung energy spectrum from the MSU experiment as shown in Fig. 10. The bremsstrahlung spectrum was obtained by GEANT4 simulations in the geometry of the experiment. The folding procedure was performed by Eq. (4)

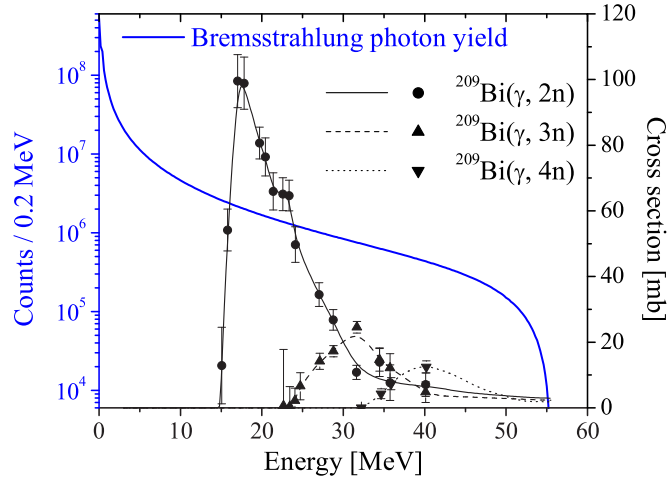


FIG. 10. The fitted and extrapolated $(\gamma,2-4n)$ cross sections and the bremsstrahlung spectrum used for the comparison with the experimental reaction yields measured by Ref. [32].

of Ref. [32], where the present fitted and extrapolated cross sections were used.

The results of the present and activation yields are listed in Table I. For all channels, the two sets of data are within the error bars. For the present yields, we assume a level of 20% uncertainty, given by the experimental error bars and by the extrapolation up to 55.6 MeV. However, we note that the central values of the present yields are systematically higher than those of the activation yields.

For the $(\gamma, 2n)$ channel we obtained a yield 25% higher than the activation yield. For this channel, only a small fraction of 15 MeV on the low-intensity bremsstrahlung spectrum has been extrapolated up to 55.6 MeV, where the high-energy tail of the cross section is strongly constrained by the highest-energy measured points. Compared with the $(\gamma, 3n)$ and $(\gamma, 4n)$ cases, the $(\gamma, 2n)$ cross-section extrapolation is more reliable, but the $(\gamma,2n)$ activation yield has higher uncertainty, because the half-life of $^{207}$Bi is of 31.5 yr and the activation method was difficult to apply. The high yield for the present cross section, which in fact is comprised of $[(\gamma, 2n) + (\gamma, 2np)]$, may suggest a high contribution from the charged particle emission channel $(\gamma,2np)$, which, because of the stable $^{206}$Pb residual nucleus, could not be measured separately using the activation technique at MSU. We note that a contribution from the $(\gamma,5np)$ channel to the $(\gamma,5n)$ channel was measured to be $36 \pm 5\%$ at MSU.

TABLE I. The experimental yields of photonuclear reactions on $^{209}$Bi measured at MSU [32] are compared with present reaction cross section data folded with the bremsstrahlung spectrum.

| Reaction | $10^{10} \times$ Yield, $C^{-1}$ | |
|---|---|---|
| | MSU [32] | Present data |
| $(\gamma,2n)$ | $2.3(2) \times 10^4$ | $2.9(6) \times 10^4$ |
| $(\gamma,3n)$ | $3.1(3) \times 10^3$ | $3.6(7) \times 10^3$ |
| $(\gamma,4n)$ | $1.02(8) \times 10^3$ | $1.1(2) \times 10^3$ |

For the $(\gamma,3n)$ channel we obtained a yield 16% higher than the activation yield. Here, the extrapolation on the high-energy region was loosely constrained by the experimental points. A slow decrease of the cross section was assumed, based on the $(\gamma,n)$ and $(\gamma,2n)$ trends at high energies. Therefore, the yield difference is more difficult to be assigned either to a high charged particle emission contribution or to a steeper cross-section decrease above 40 MeV. We note that the $(\gamma,3np)$ channel could not be measured by activation technique at MSU because of the long half-life of $1.7 \times 10^7$ yr for the residual nucleus $^{205}$Pb.

For the $(\gamma,4n)$ channel the present yield is within one standard deviation from the activation yield. A small contribution of less the 1% of the $(\gamma,4n)$ channel was separately measured at MSU for the charged particle channel $(\gamma,4np)$, therefore we can directly compare the activation and present yields for the $(\gamma,4n)$ reaction. Here, the 8% difference between the two values is most likely given by the uncertain extrapolation up to 55.6 MeV. Following statistical model calculations, we assumed that the last data point at 40 MeV represents the peak cross section of the $(\gamma,4n)$ channel.

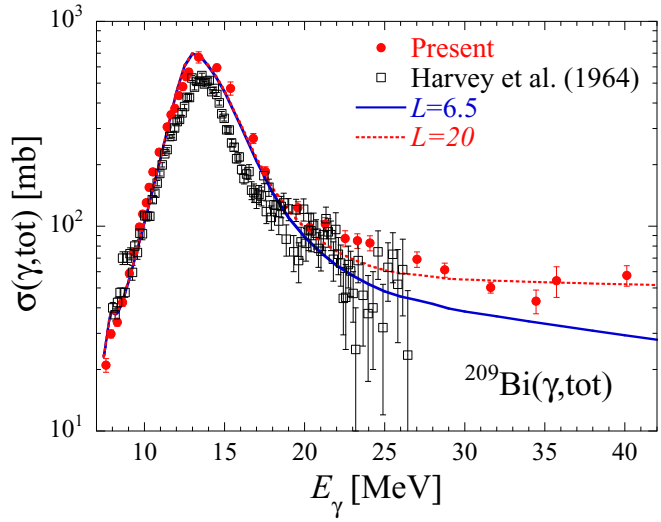


FIG. 11. Comparison of our total experimental cross section $\sigma(\gamma,\text{tot}) = \sum_{x=1}^{4} \sigma(\gamma,\text{xn})$ with previous measurements [30] and with the TALYS predictions for two values of the Levinger parameter $L = 6.5$ (solid line) and $L = 20$ (dashed line).

## V. THEORETICAL INTERPRETATION

### A. Total and partial photoneutron cross sections

The experimental photoneutron cross sections $^{209}$Bi$(\gamma,xn)$ are now compared with theoretical calculations obtained with the TALYS reaction code [43]. The total absorption cross section is traditionally given by

$$\sigma_{\text{abs}}(E_\gamma) = \sigma_{\text{GDR}}(E_\gamma) + \sigma_{\text{QD}}(E_\gamma), \tag{7}$$

where $\sigma_{\text{GDR}}$ is the giant dipole resonance (GDR) contribution estimated here within the Hartree-Fock-Bogolyubov plus quasiparticle random phase approximation (HFB+QRPA) approach on the basis of the D1M Gogny interaction, both for the $E1$ [48] and $M1$ [49] components. The $\sigma_{\text{QD}}$ cross section corresponds to the quasideuteron component [50–52] obtained from the standard expression

$$\sigma_{\text{QD}}(E_\gamma) = L\frac{NZ}{A}\sigma_d(E_\gamma)f(E_\gamma), \tag{8}$$

where $\sigma_d$ is the experimental deuteron photodisintegration cross section, $f(E_\gamma)$ the Pauli-blocking function and $L$ the so-called Levinger parameter. Note that the reduction factor $L/A$ in Eq. (8) accounts for the fact that only correlated pairs can be considered to be quasideuterons. While for photon energy $E_\gamma \leqslant 20$ MeV, the cross section is dominated by the equilibrium Hauser-Feshbach component related to the GDR contribution, at higher energies the quasideuteron contribution in the preequilibrium mode dominates.

We compare in Fig. 11 the total experimental cross section $\sigma(\gamma,\text{tot}) = \sum_{i=1}^{4} \sigma(\gamma,\text{in})$ with previous measurements [29,30] and with the default TALYS calculations obtained with the standard Levinger parameter $L = 6.5$ [50,51]. The total cross section is given by Eq. (7) and remains independent of the outgoing channel description (note that the contribution involving the photoemission of protons is found theoretically to be relatively small and not to change the present conclusions drawn on the total photoabsorption cross section). The present measurements agree relatively well with previous measurements [29,30] although we obtain higher cross sections around the GDR peak energy and lower between 18 and 25 MeV. The GDR properties around the peak energy correspond to a standard Lorentzian of centroid energy $E_0 = 13.7$ MeV, full width at half maximum $\Gamma_0 = 4.5$ MeV, and peak cross section $\sigma_0 = 680$ mb. The GDR region is found to be rather well described by the HFB+QRPA model [48,49], both at the neutron threshold and within the GDR region. In particular, the $(\gamma,n)$ cross section just above the neutron threshold at an energy $E_\gamma \simeq 8$ MeV shows a relative increase (see also Fig. 11) that is explained by the HFB+QRPA calculations through the presence of the $M1$ spin-flip resonance [49].

However, at energies above 20 MeV, the default TALYS calculation, essentially dominated by the quasideuteron contribution with standard value of $L \sim 6.5$, underestimates the measured cross section. Keeping the same expression for the Pauli-blocking function [51], a value of $L$ about three times larger is needed to reproduce the large total cross section at energies between 20 and 40 MeV (Fig. 11). Our large experimental cross section (also confirmed by the previous measurements around 20–25 MeV [29,30]) is at 40 MeV about three times larger than the 15 mb photoabsorption cross section previously measured in the neighboring nucleus $^{208}$Pb [53] and stems from the relatively large $(\gamma,1n)$ contribution, as seen in Fig. 12. The $L$ parameter used in previous analyses of the total photoabsorption was limited to the 5–10 range [50,51], essentially due to the ambiguity between the $L$ parameter and the adopted Pauli-blocking function. However, the Pb-Bi discrepancy at 40 MeV remains and our present large $(\gamma,n)$ cross section above 20 MeV remains difficult to understand in the present standard knowledge.

While the default TALYS preequilibrium calculation of the total $(\gamma,\text{tot})$ cross section can be improved by increasing the Levinger parameter (Fig. 11), at high energies, the partial

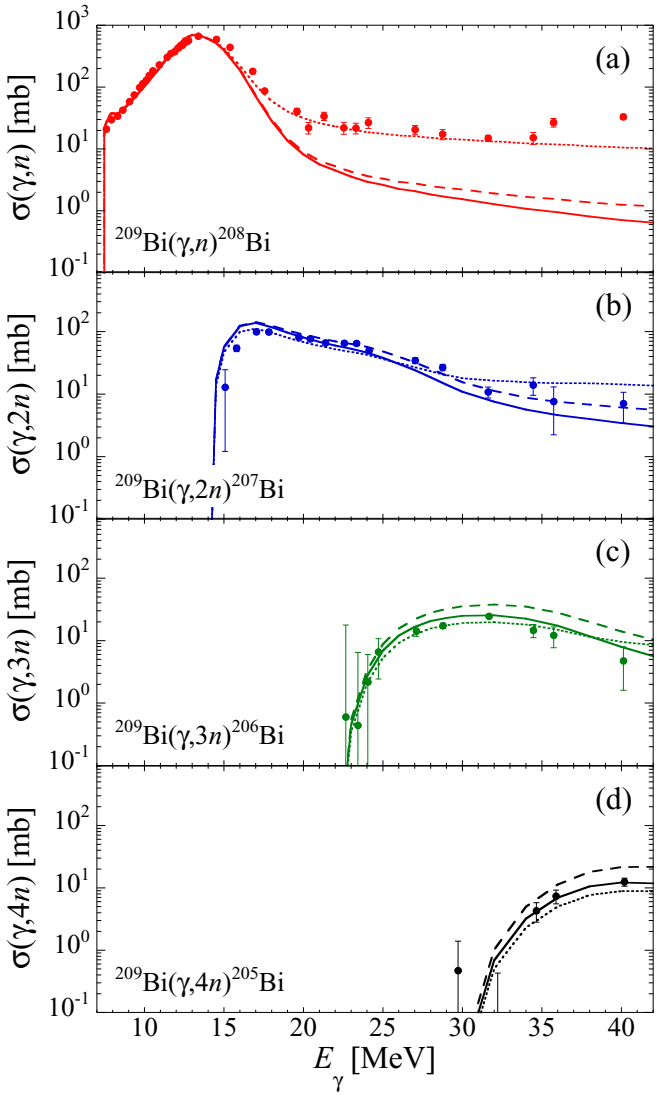


FIG. 12. Comparison of the experimental partial cross section $\sigma(\gamma,xn)$ ($x = 1$–4) with the TALYS calculation obtained with the default preequilibrium parametrization (solid lines), the modified parameter $L = 20$ but no surface effects (dashed lines) and $L = 20$ with surface effects ($E_{\rm surf} = 1$ MeV) (dotted lines).

$(\gamma,n)$ cross section remains underestimated and the $(\gamma,2n)$ and $(\gamma,3n)$ cross sections tend to be overestimated, as shown by the dashed lines in Fig. 12. All channels $(\gamma,xn)$ ($x = 1$–4) can be rather well reproduced by including a surface contribution to the finite well depth of the two-component particle-hole state density [54]. Although the standard photoneutron cross-section calculation neglects the surface contribution for photoneutron reactions, we found that including such an effect with a low surface energy $E_{\rm surf} = 1$ MeV affects the particle-hole state densities, hence the emission rates significantly, as seen in Fig. 12. This surface effect reduces the maximum depth of the effective potential in which a hole can be created leaving, for the first stage, more energy to be adopted by the excited particle and yielding more emission at the highest outgoing energies. This modification together with a high $L$ parameter increase the $(\gamma,xn)$ cross section

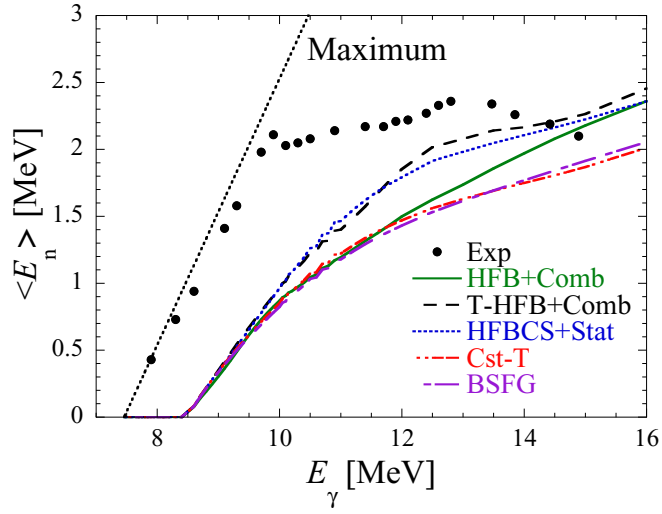


FIG. 13. Comparison of the experimental average energy of the emitted neutrons $\langle E_n \rangle$ as a function of the photon energy with the TALYS estimates obtained with different nuclear level density descriptions [56–59] of the low-lying states in $^{208}$Bi. The dotted black curve referred to as "Maximum" corresponds to the emission of neutrons directly and uniquely to the ground state of $^{208}$Bi.

at energies above which the photoemission of $x + 1$ neutrons starts to dominate. This modified preequilibrium photoneutron calculation reproduces relatively well the measurements above 20 MeV, as illustrated by the dotted lines in Fig. 12.

We remark that the large $(\gamma,n)$ cross section above 20 MeV could be explained in terms of a significant decrease of the energy-dependent spreading width of the GDR states within the framework of the combined photonucleon-reaction model (CM) [55]. A decreased spreading width can make the GDR spend more time at the $1p1h$ state to relatively enhance decays to the $(\gamma,n)$ channel and leads to an even longer-lived collective nature of the GDR. As a result, the model suggests to enhance the high-energy tail of the GDR and thus, the photoabsorption cross section. However, this picture remains also inconsistent with the measured $(\gamma,n)$ cross section of $^{208}$Pb at high energy [53]. We will present details of the CM model calculation in a separate paper.

### B. Threshold behavior of photoneutron emission

In Fig. 13, the experimental average energy of the emitted neutrons is plotted as a function of the photon energy and compared with the TALYS prediction. The experimental average neutron energy is seen to be significantly larger than the predicted one reaching at energies below 10 MeV almost the largest possible energy corresponding to the emission of neutrons directly to the ground state of $^{208}$Bi, i.e. $\langle E_n \rangle = (A-1)/A \times (E_\gamma - S_n)$. The emission of $s$-wave neutrons from $E1$ photoexcited states in $^{209}$Bi mainly populates the $3^+$ to $6^+$ levels in $^{208}$Bi. Levels with such spins and parity are known experimentally in $^{208}$Bi up to energies of about 1.5 MeV, so that it remains difficult to explain within the statistical model that essentially only high-energy neutrons to the ground state are emitted or that no thermodynamic

equilibrium of the compound system is achieved at these energies. For energies $E_\gamma > 10$ MeV, the average neutron energy becomes sensitive to the adopted nuclear level density in $^{208}$Bi, as shown in Fig. 13 where the various models [56–59] are found to predict a different number of $J^\pi = 3^+$–$6^+$ levels. The lower the density of these levels, the higher the average energy of the emitted neutrons. A similar underestimate of the average neutron energy is also obtained with the reaction code EMPIRE [44] or CoH3 [42]. The present measurement remains theoretically puzzling unless spin-flip $M1$ excitations followed by $p$-wave neutron emissions to the ground state through the centrifugal potential dominate immediately above neutron threshold. A photoneutron experiment with a linearly polarized $\gamma$-ray beam [17] is desirable to investigate $E1$ and $M1$ excitations in $^{209}$Bi above the neutron threshold.

## VI. CONCLUSIONS

Total and partial photoneutron cross sections with neutron multiplicity 1–4 were measured for $^{209}$Bi by direct neutron-multiplicity sorting with a flat-response neutron detector, which was devised as a technical foundation of resolving the longstanding discrepancy between the Livermore and Saclay data of photoneutron cross sections. The data were discussed with the HFB+QRPA model for the GDR component based on the Gogny D1M interaction for both $E1$ and $M1$ excitations and the standard prescription for the QD component with the Levinger parameter. The new data have raised an important discussion on the origin of the total photoneutron cross section at high energy, which is characterized by a survival of large $(\gamma,n)$ cross sections above 20 MeV, either the QD with an enhanced Levinger parameter or GDR with a reduced spreading width. Our subsequent measurements will contribute to this important issue. This is the first of a series of measurements involving 11 nuclei from $^{9}$Be to $^{209}$Bi dedicated to the IAEA-CRP on updating the photonuclear data library, IAEA-TECDOC-1178.

## ACKNOWLEDGMENTS

I.G. and D.F. acknowledge the support from the Extreme Light Infrastructure Nuclear Physics (ELI-NP) Phase II, a project cofinanced by the Romanian Government and the European Union through the European Regional Development Fund - the Competitiveness Operational Programme (1/07.07.2016, COP, ID 1334). S.G. acknowledges the support from the F.R.S.-FNRS. H.U. acknowledges the support from the Premier Project of the Konan University. K.S. and S.B. acknowledge support from the Russian Foundation for Basic Research (Grant No. 15-02-05939). This work was supported by the IAEA under Contracts No. ROM-20476, No. RUS-20501, and No. JPN-20564 for the CRP F41032 on Updating the Photonuclear Data Library.

[1] S. S. Dietrich and B. L. Berman, At. Data Nucl. Data Tables **38**, 199 (1988).
[2] IAEA Photonuclear Data Library, https://www-nds.iaea.org/photonuclear/.
[3] B. S. Ishkhanov *et al.*, Phys. At. Nucl. **67**, 1664 (2004).
[4] IAEA Coordinated Research Project on Photonuclear Data and Photon Strength Functions, https://www-nds.iaea.org/CRP-photonuclear/.
[5] H. Ohgaki *et al.*, IEEE Trans. Nucl. Sci. **38**, 386 (1991).
[6] H. Utsunomiya, Y. Yonezawa, H. Akimune, T. Yamagata, M. Ohta, M. Fujishiro, H. Toyokawa, and H. Ohgaki, Phys. Rev. C **63**, 018801 (2000).
[7] H. Utsunomiya, H. Akimune, S. Goko, M. Ohta, H. Ueda, T. Yamagata, K. Yamasaki, H. Ohgaki, H. Toyokawa, Y. W. Lui, T. Hayakawa, T. Shizuma, E. Khan, and S. Goriely, Phys. Rev. C **67**, 015807 (2003).
[8] K. Y. Hara, H. Utsunomiya, S. Goko, H. Akimune, T. Yamagata, M. Ohta, H. Toyokawa, K. Kudo, A. Uritani, Y. Shibata, Y. W. Lui, and H. Ohgaki, Phys. Rev. D **68**, 072001 (2003).
[9] T. Shizuma, H. Utsunomiya, P. Mohr, T. Hayakawa, S. Goko, A. Makinaga, H. Akimune, T. Yamagata, M. Ohta, H. Ohgaki, Y. W. Lui, H. Toyokawa, A. Uritani, and S. Goriely, Phys. Rev. C **72**, 025808 (2005).
[10] H. Utsunomiya, A. Makinaga, S. Goko, T. Kaihori, H. Akimune, T. Yamagata, M. Ohta, H. Toyokawa, S. Muller, Y. W. Lui, and S. Goriely, Phys. Rev. C **74**, 025806 (2006).
[11] H. Utsunomiya, S. Goriely, T. Kondo, T. Kaihori, A. Makinaga, S. Goko, H. Akimune, T. Yamagata, H. Toyokawa, T. Matsumoto, H. Harano, S. Hohara, Y. W. Lui, S. Hilaire, S. Peru, and A. J. Koning, Phys. Rev. Lett. **100**, 162502 (2008).
[12] H. Utsunomiya, S. Goriely, M. Kamata, T. Kondo, O. Itoh, H. Akimune, T. Yamagata, H. Toyokawa, Y. W. Lui, S. Hilaire, and A. J. Koning, Phys. Rev. C **80**, 055806 (2009).
[13] H. Utsunomiya, S. Goriely, H. Akimune, H. Harada, F. Kitatani, S. Goko, H. Toyokawa, K. Yamada, T. Kondo, O. Itoh, M. Kamata, T. Yamagata, Y. W. Lui, I. Daoutidis, D. P. Arteaga, S. Hilaire, and A. J. Koning, Phys. Rev. C **82**, 064610 (2010).
[14] A. Makinaga, H. Utsunomiya, S. Goriely, T. Kaihori, S. Goko, H. Akimune, T. Yamagata, H. Toyokawa, T. Matsumoto, H. Harano, H. Harada, F. Kitatani, Y. K. Hara, S. Hohara, and Y. W. Lui, Phys. Rev. C **79**, 025801 (2009).
[15] F. Kitatani *et al.*, J. Korean Phys. Soc. **59**, 1836 (2011).
[16] O. Itoh *et al.*, J. Nucl. Sci. Technol. **48**, 834 (2011).
[17] T. Kondo, H. Utsunomiya, S. Goriely, I. Daoutidis, C. Iwamoto, H. Akimune, A. Okamoto, T. Yamagata, M. Kamata, O. Itoh, H. Toyokawa, Y. W. Lui, H. Harada, F. Kitatani, S. Hilaire, and A. J. Koning, Phys. Rev. C **86**, 014316 (2012).
[18] C. T. Angell, S. L. Hammond, H. J. Karwowski, J. H. Kelley, M. Krticka, E. Kwan, A. Makinaga, and G. Rusev, Phys. Rev. C **86**, 051302(R) (2012).
[19] H. Utsunomiya, S. Goriely, T. Kondo, C. Iwamoto, H. Akimune, T. Yamagata, H. Toyokawa, H. Harada, F. Kitatani, Y. W. Lui, A. C. Larsen, M. Guttormsen, P. E. Koehler, S. Hilaire, S. Peru, M. Martini, and A. J. Koning, Phys. Rev. C **88**, 015805 (2013).
[20] S. Amano *et al.*, Nucl. Instrum. Methods A **602**, 337 (2009).
[21] D. M. Filipescu, I. Gheorghe, H. Utsunomiya, S. Goriely, T. Renstrom, H. T. Nyhus, O. Tesileanu, T. Glodariu, T. Shima, K. Takahisa, S. Miyamoto, Y. W. Lui, S. Hilaire, S. Peru, M. Martini, and A. J. Koning, Phys. Rev. C **90**, 064616 (2014).

[22] H. T. Nyhus, T. Renstrom, H. Utsunomiya, S. Goriely, D. M. Filipescu, I. Gheorghe, O. Tesileanu, T. Glodariu, T. Shima, K. Takahisa, S. Miyamoto, Y. W. Lui, S. Hilaire, S. Peru, M. Martini, L. Siess, and A. J. Koning, Phys. Rev. C **91**, 015808 (2015).
[23] T. Renstrom, H. T. Nyhus, H. Utsunomiya, R. Schwengner, S. Goriely, A. C. Larsen, D. M. Filipescu, I. Gheorghe, L. A. Bernstein, D. L. Bleuel, T. Glodariu, A. Gorgen, M. Guttormsen, T. W. Hagen, B. V. Kheswa, Y. W. Lui, D. Negi, I. E. Ruud, T. Shima, S. Siem, K. Takahisa, O. Tesileanu, T. G. Tornyi, G. M. Tveten, and M. Wiedeking, Phys. Rev. C **93**, 064302 (2016).
[24] H. Utsunomiya, S. Katayama, I. Gheorghe, S. Imai, H. Yamaguchi, D. Kahl, Y. Sakaguchi, T. Shima, K. Takahisa, and S. Miyamoto, Phys. Rev. C **92**, 064323 (2015).
[25] C. W. Arnold, T. B. Clegg, C. Iliadis, H. J. Karwowski, G. C. Rich, J. R. Tompkins, and C. R. Howell, Phys. Rev. C **85**, 044605 (2012).
[26] H. Utsunomiya *et al.*, Nucl. Instrum. Methods A **871**, 135 (2017).
[27] *Lead-bismuth Eutectic Alloy Handbook*, Nuclear Energy Agency No. 7268, OECD (2015).
[28] R. Capote *et al.*, J. ASTM Int. **9**, 104119 (2012).
[29] J. Miller, C. Schuhl, and C. Tzara, Nucl. Phys. **32**, 236 (1962).
[30] R. R. Harvey, J. T. Caldwell, R. L. Bramblett, and S. C. Fultz, Phys. Rev. **136**, B126 (1964).
[31] Yu. I. Sorokin *et al.*, Izv. Ross. Akad. Nauk, Ser. Fiz. **37**, 1890 (1973).
[32] S. S. Belyshev *et al.*, Eur. Phys. J. A **51**, 67 (2015).
[33] H. Utsunomiya *et al.*, IEEE Trans. Nucl. Sci. **61**, 1252 (2014).
[34] T. Shima and H. Utsunomiya, in *Proceedings of the Nuclear Physics and Gamma-ray Sources for Nuclear Security and Nonproliferation, Tokai, Japan*, edited T. Hayakawa *et al.* (World Scientific Publishing, Singapore, 2014), pp. 151–160.
[35] J. Allison *et al.*, IEEE Trans. Nucl. Sci. **53**, 270 (2006).
[36] K. Horikawa *et al.*, Nucl. Instrum. Methods A **618**, 209 (2010).
[37] University of Hyogo, NewSUBARU Synchrotron Radiation Facility, http://www.lasti.u-hyogo.ac.jp/NS-en/facility/ring/para.html.
[38] T. Kondo *et al.*, Nucl. Instrum. Methods A **659**, 462 (2011).
[39] J. F. Briesmeister, Computer code MCNP, Version 4C (Los Alamos National Laboratory, Los Alamos, 2000).
[40] V. Weisskopf, Phys. Rev. **52**, 295 (1937).
[41] B. L. Berman and S. C. Fultz, Rev. Mod. Phys. **47**, 713 (1975).
[42] T. Kawano *et al.*, J. Nucl. Sci. Technol. **47**, 462 (2010).
[43] A. J. Koning and D. Rochman, Nucl. Data Sheets **113**, 2841 (2012).
[44] M. Herman, R. Capote, B. V. Carlson, P. Oblozinsky, M. Sin, A. Trkov, H. Wienke, and V. Zerkin, Nucl. Data Sheets **108**, 2655 (2007).
[45] NIST Physical Measurement Laboratory, http://physics.nist.gov/PhysRefData/Xcom/html/xcom1.html.
[46] NIST Physical Measurement Laboratory, http://physics.nist.gov/PhysRefData/XrayMassCoef/tab1.html.
[47] A. Ermakov *et al.*, Proc. XXIII Russian Particle Accelerator Conference RuPAC-2012, p. 538.
[48] M. Martini, S. Peru, S. Hilaire, S. Goriely, and F. Lechaftois, Phys. Rev. C **94**, 014304 (2016).
[49] V. Tselyaev, N. Lyutorovich, J. Speth, S. Krewald, and P. G. Reinhard, Phys. Rev. C **94**, 034306 (2016).
[50] M. L. Terranova, D. A. De Lima, and J. D. Pinheiro Filho, Europhys. Lett. **9**, 523 (1989).
[51] M. B. Chadwick, P. Oblozinsky, P. E. Hodgson, and G. Reffo, Phys. Rev. C **44**, 814 (1991).
[52] *Handbook on photonuclear data for applications: Cross sections and spectra*, IAEA-TECDOC-1178, 2000.
[53] A. Lepretre *et al.*, Nucl. Phys. A **367**, 237 (1981).
[54] A. J. Koning and M. C. Duijvestijn, Nucl. Phys. A **744**, 15 (2004).
[55] B. S. Ishkhanov and V. N. Orlin, Phys. At. Nucl. **78**, 557 (2015).
[56] A. J. Koning, S. Hilaire, and S. Goriely, Nucl. Phys. A **810**, 13 (2008).
[57] S. Goriely, S. Hilaire, and A. J. Koning, Phys. Rev. C **78**, 064307 (2008).
[58] R. Capote, M. Herman, P. Oblozinsky *et al.*, Nucl. Data Sheets **110**, 3107 (2009).
[59] S. Hilaire, M. Girod, S. Goriely, and A. J. Koning, Phys. Rev. C **86**, 064317 (2012).